physica status solidi a
www.pss-a.com

Lattice Dynamics of $LiNb_{1-x}Ta_xO_3$ Solid Solutions: Theory and Experiment

Felix Bernhardt, Soham Gharat, Alexander Kapp, Florian Pfeiffer, Robin Buschbeck, Franz Hempel, Oleksiy Pashkin, Susanne C. Kehr, Michael Rüsing, Simone Sanna, and Lukas M. Eng*

Lithium niobate (LNO) and lithium tantalate (LTO) see widespread use in fundamental research and commercial technologies reaching from electronics over classical optics to integrated quantum communication. The mixed crystal system lithium niobate tantalate (LNT) allows for the dedicate engineering of material properties by combining the advantages of the two parental materials LNO and LTO. Vibrational spectroscopies such as Raman spectroscopy or (Fourier transform) infrared (IR) spectroscopy are vital techniques to provide detailed insight into the material properties, which is central to the analysis and optimization of devices. This work presents a joint experimental–theoretical approach allowing to unambiguously assign the spectral features in the LNT material family through both Raman and IR spectroscopy, as well as providing an in-depth explanation for the observed scattering efficiencies based on first-principles calculations. The phononic contribution to the static dielectric tensor is calculated from the experimental and theoretical data using the generalized Lyddane–Sachs–Teller relation and compared with the results of the first-principles calculations.

1. Introduction

Lithium niobate ($LiNbO_3$, LNO) and lithium tantalate ($LiTaO_3$, LTO) are two isomorphous ferroelectrics (space group $R3_c$) and are among the most widely used materials in electro-optic applications.[1–3] Both materials feature a ferroelectric-to-paraelectric structural phase transition, which, according to the recent knowledge, is a phase transition of second order.[4,5] Correspondingly, the spontaneous polarization P_S steadily increases with decreasing temperature from 0 at the Curie temperature to a value of 71(62) and 60(55) μC cm^{-2} for congruent (nearly stoichiometric) LNO[6] and LTO[7] at low temperatures, respectively. LNO and LTO are birefringent, and have useful acoustic wave properties[8] and a rather large acousto-optic figure-of-merit. The wealth of physical effects and, more importantly, their magnitude render LNO and LTO ideal candidates for acoustic and optical applications, exploiting both their bulk and surface properties.[9,10] LNO is characterized by unusually large pyroelectric, piezoelectric, electro-optic, and photoelastic coefficients.[1] The magnitude of these coefficients is less pronounced in LTO, which features, however, higher thermal stability due to, for example, lower thermally activated conductivity, which is favorable for high-temperature sensing applications.[11] In contrast, however, LTO has a much lower Curie temperature compared to LNO (874–958 K for LTO[6,12] vs 1413–1475 K for LNO),[7,13] limiting its applications to lower temperature regions. Thus, both LNO and LTO feature different, restraining characteristics for high-temperature applications. Recently, lithium niobate tantalate solid solutions ($LiNb_{1-x}Ta_xO_3$, LNT) have gained attention, as they conjugate the favorable properties of LNO with the thermal stability of

F. Bernhardt, A. Kapp, F. Pfeiffer, S. Sanna
Institut für Theoretische Physik
Center for Materials Research (LaMa)
Justus-Liebig-Universität Giesen
35392 Giesen, Germany
E-mail: felix.bernhardt@theo.physik.uni-giessen.de

The ORCID identification number(s) for the author(s) of this article can be found under https://doi.org/10.1002/pssa.202300968.

DOI: 10.1002/pssa.202300968

S. Gharat, R. Buschbeck, F. Hempel, S. C. Kehr, M. Rüsing, L. M. Eng
Institut für Angewandte Physik
Technische Universität Dresden
01062 Dresden, Germany

O. Pashkin
Spectroscopy Department
Helmholtz-Zentrum Dresden-Rossendorf
01328 Dresden, Germany

M. Rüsing
Integrated Quantum Optics
Institute for Photonic Quantum Systems (PhoQS)
Paderborn University
Warburger Str. 100, 33098 Paderborn, Germany

L. M. Eng
ct.qmat: Dresden-Würzburg Cluster of Excellence—EXC 2147
TU Dresden
01062 Dresden, Germany

LTO.[11,14–16] Furthermore, LNT solid solutions allow for the tailoring of many material properties by adjusting the niobium–tantalum ratio and/or the Li concentration.[14–18]

For a complete characterization regarding the niobium/tantalum ratio of the LNT solid solution, the knowledge of the dynamical properties of the crystal lattice of the end compounds LNO and LTO is crucial. Indeed, it bears information concerning, e.g., crystal symmetry, phase transition dynamics, and many other aspects. In this context, Raman spectroscopy and the complementary infrared (IR) spectroscopy both provide access to study the dynamical properties of the lattice and, in turn, to characterize many fundamental material parameters.[17,19]

Many different studies did focus on the investigation of the phonon modes of LNO and LTO.[20–30] These investigations lead to the assignment of the experimentally detected spectral signatures associated with atomic displacement patterns. However, the data from the literature present a not fully consistent picture. In particular, in the case of LNO, there have been many ambiguities in the assignment of spectral features regarding, e.g., the E-$TO_{5,6}$ (transverse optical), E-TO_9, or E-LO (longitudinal optical) mode frequencies.[19,20,24,31] Moreover, the knowledge of the dynamical properties of the solid solutions is rather limited despite decades of research.[17,19,32]

Here, we investigate the dynamical properties of $LiNb_{1-x}Ta_xO_3$ solid solutions and their end compounds both theoretically and experimentally. LO and TO phonon frequencies, IR spectra—more precisely the complex dielectric function—and Raman spectra are calculated from first principles within density functional theory (DFT) and compared to experimental data obtained by both Fourier-transform infrared (FTIR) spectroscopy and μ-Raman spectroscopy, using the exact same samples and experimental setups for LNO, LTO, and an LNT crystal.

Raman and FTIR spectroscopy are complementary techniques that, relying on different physical processes, give access to phonon modes of different symmetry in some materials or, in the case of LNO and LTO, enable a much improved assignment of phonons, as some have a very low scattering efficiency in either Raman or IR. Calculated and experimentally observed phonon modes are compared to each other and, where existing, with available literature data. This allows for the assignment and determination of all optical phonon modes, including some that are difficult to measure solely by Raman or (FT)IR spectroscopies. The selection rules for Raman and IR activity of stoichiometric LNO and LTO are discussed in detail, and it is pointed out how these rules are lifted due to the local deformations present in the LNT solid solutions. Finally, the measured phonon frequencies are employed to estimate the phononic contribution to the dielectric tensor with the Lyddane–Sachs–Teller (LST) relation.[33,34]

2. Experimental Section

2.1. Samples

In this work, we have investigated three types of single crystals: 1) LNO, 2) LTO, and 3) LNT mixed crystals with a tantalum concentration of $x = 0.70 \pm 0.03$. LNO and LTO crystals are grown at their congruent point, i.e., all crystals feature the typical lithium deficiency of ≈1.5 mol%, which is a result of the crystal growth technique.[3] We assume a similar lithium deficiency for our LNT crystals due to similar growth conditions.[14] The crystals are otherwise undoped. The LNO and LTO crystals are commercially obtained (Impex HighTech GmbH, Münster, Germany), while the LNT crystals were grown by the Czochralski method at the Leibniz Institute for Crystal Growth, IKZ, Berlin. The growth of the LNT crystals is described elsewhere.[14] The crystal orientation has been determined via X-ray diffraction and samples have been prepared as *x*-cut, *y*-cut, or *z*-cut, which allows to study all optically active phonon branches, as well as transverse- and longitudinal-polarized phonon modes. All crystal surfaces, which have been studied in Raman or FTIR spectroscopy, have been polished to optical quality.

2.2. Raman Spectroscopy

Raman spectroscopy was carried out on a LabRAM HR Evolution Raman spectroscope by Horiba Seisakusho. Excitation light is provided by a linearly polarized 17 mW HeNe laser at 632.8 nm. The laser light is focused via an objective lens with a low numerical aperture of 0.3. No confocal pinhole is inserted in the detection path. The low numerical aperture and the omission of a confocal pinhole allow one to average the signal over a larger sample volume, and it reduces the influence of focusing-related depolarization.[35] The scattered light is collected in back-reflection geometry via the same objective lens. The elastically scattered light is blocked via an appropriate edge filter and spectral analysis is performed in an attached spectrometer with a 600 grooves/mm grating and detected with a charge-coupled device. The setup reaches a spectral resolution better than 2 cm^{-1}. The light polarization in excitation and detection paths is set by automatized half-wave plates and linear polarizers, respectively. Calibration was done by measuring (100)-cut single-crystalline silicon, which shows one prominent and sharp peak at 521 cm^{-1}. More details on the setup can be found elsewhere.[36]

For each sample and available crystal orientation, polarized Raman spectra are recorded by placing the focus more than 10 μm below the surface to limit spectroscopic signatures from the surface. Due to the high Raman scattering efficiency in the LNT crystal family, high signal-to-noise ratio Raman spectra, which require no further smoothing, can be obtained with integration times of a few seconds at most. The obtained spectra are normalized to their respective maximum after the dark counts have been subtracted. No further data processing was performed for joint plotting with the calculated spectra. To accurately extract the peak frequencies, the spectra were fitted with Lorentzian functions.

2.3. FTIR Spectroscopy

Reflectance FTIR spectroscopy is performed on a Bruker VERTEX 80v FTIR spectrometer in the range from 50 to about 1000 cm^{-1}, covering the known phononic frequencies of LNO and LTO.[20] The light is focused and collected via two ellipsoidal mirrors, which are aligned to a common focus. The spectrometer yields a spectral resolution of about 4 cm^{-1}. Reference reflectance spectra are taken on a gold reference mirror. The light polarization of the globar source is set linear with a Tydex thin-film wire-grid polarizer.

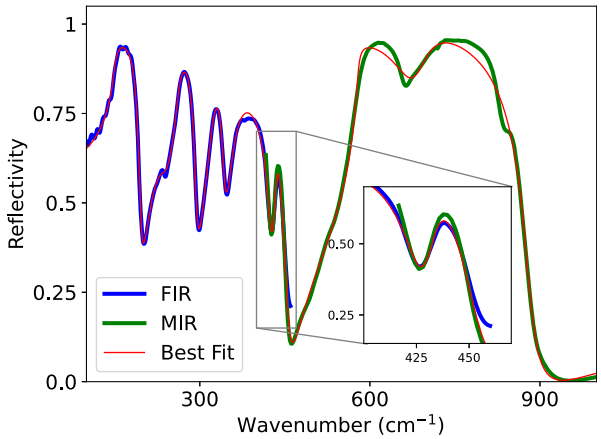

Figure 1. Exemplary FTIR reflectance spectrum of the *z*-cut LNO sample in ordinary light polarization (E||*x*). Due to limitations in the experimental setup, the spectra are measured with two different beam splitter/detector combinations, one operating in the FIR region displayed in blue and one operating in the MIR range displayed in green. The spectra show a good overlap in the 400–450 cm^{-1} range, which is used to merge the two datasets. To extract the full dielectric function in the phononic range, the spectrum is fitted with an oscillator model as shown in Equation 1. The best fit for the given spectrum is shown in red.

Figure 1 shows an exemplary raw dataset taken on *z*-cut LNO, where the light is polarized along the extraordinary axis of the crystal (E||*x*). Due to the limited spectral range of the available beam splitters, two different experimental settings for the mid-infrared (MIR; 400–1000 cm^{-1}, Ge/KBr beam splitter, MIR-BLATGS detector) and far-infrared (FIR, 50–600 cm^{-1}, Mylar beam splitter, FIR-DTGS detector) were used to measure the full range of phonon frequencies in the LNT crystal family. This can be readily seen in the raw data in Figure 1, where the FIR data are displayed in blue and the MIR data in green. The two ranges show a good overlap in the 400–450 cm^{-1} range, as displayed in the inset, which is used to merge the datasets.

To obtain the dielectric function $\varepsilon(\omega)$ in the phononic frequency range, the obtained reflectance spectrum is fitted with a four parameter oscillator model of the form

$$\varepsilon(\omega) = \varepsilon_\infty \prod_{j=1}^{n} \frac{\omega_{\mathrm{LO}j}^2 - \omega^2 + i\omega\gamma_{\mathrm{LO}j}}{\omega_{\mathrm{TO}j}^2 - \omega^2 + i\omega\gamma_{\mathrm{TO}j}}. \quad (1)$$

In this equation, the $4n+1$ independent (fitting) parameters are $\omega_{\mathrm{LO}j}$ and $\omega_{\mathrm{TO}j}$, which refer to the frequencies of the *j*th LO and TO phonon modes, respectively, and $\gamma_{\mathrm{LO}j}$ and $\gamma_{\mathrm{TO}j}$, which refer to their respective damping constants, as well as the high-frequency permittivity ε_∞, which describes the dielectric contribution of the electronic background, which becomes dominant at higher frequencies (toward optical frequencies).

Compared to a more traditional three-parameter Drude–Lorentz oscillator model, which features only one damping constant and was used in the past for LNO or LTO,[37] fitting the four parameter model was chosen because it describes the dielectric functions of materials with a strong LO–TO splitting commonly seen in polar crystals, like ferroelectrics, more accurately.[38,39] Furthermore, in the limit of $\omega \to 0$ Equation (1) is identical to the LST relation in Equation (8).

The fitting procedure of the reflectance spectrum is performed via the software RefFIT,[40] yielding the real ε' and imaginary ε'' contributions of the dielectric function. A fitting result is displayed in Figure 1, which shows a good agreement with the raw data. Subsequently in this work, only the extracted real ε' and imaginary ε'' dielectric function are shown. Prior to fitting of each datasets, the number of expected phonons is set. Approximate starting frequencies are based on the literature or Raman data. Specifically, in datasets containing A_1-symmetry phonons, we did set four phonons of A_1 type. However, for E-type symmetry phonons we only used eight instead of nine independent phonons because from the previous work it is known that the E-TO$_6$ has a very weak IR oscillator strength and is spectrally very close (10 cm^{-1}) to the more intense E-TO$_5$.[19,24,32] This is reversed in Raman spectroscopy, where the E-TO$_5$ is quasi-Raman silent and dominated by the E-TO$_6$, as also confirmed by theoretical calculations (Section 4.2).

2.4. Phonon Modes and Selection Rules

LNO and LTO are isostructural with two formula units per unit cell. This results in 27 optical phonon modes. Based on group theory, the optical phonon modes at the Brillouin zone center Γ are further subdivided in four modes of A_1-type, five modes of A_2-type, and nine doubly degenerate modes of E-type symmetry. Only the A_1 and E-symmetry phonons are Raman and IR-active, while the A_2 phonons are optically silent. Furthermore, each phonon may be associated with a transverse optical frequency and a longitudinal optical frequency, as discussed in Equation (1), which define the Reststrahlen band in the reflectance spectra. Therefore, to characterize the full optical response either by Raman or IR spectroscopy, four A_1-TO and four A_1-LO frequencies, as well as nine E-TO and nine E-LO frequencies, need to be known. In the LNO crystal system, it is common to label the phonons in ascending order, e.g., E-LO$_6$ refers to the sixth highest frequency E-type symmetry LO phonon.

As discussed below (Section 3.1), the mixed crystals cannot be described by the same unit cell due to the larger supercell necessary to take into account the arbitrary Nb–Ta content of the mixed crystals. Assuming the natural randomness in the Nb–Ta distribution, a large number of phonons will be present at the Brillouin-zone center, leading to a natural broadening of peaks and a lifting of the selection rules. Therefore, strictly speaking, the selection rules, which are true for the end compounds LNO and LTO, are not necessarily valid for the mixed crystals. Nevertheless, we chose to label the features in the mixed crystals only with a single mode in accordance with its closest phononic analogue in the end compound. These quasi A_1 and E-modes are labeled with a prime, e.g., A_1'-TO$_1$ denoting the peak that behaves similar in terms of selection rule to the A_1-TO$_1$ mode in either the LNO or LTO end compounds.

The selection rules in Raman spectroscopy can be calculated based on the known Raman tensors, which summarizes the propagation direction of the phonons to distinguish both LO and TO phonons, and assign which phonons for a given set of excitation and detection light polarization can be detected.

Table 1. Observable phonon modes and Raman tensor elements recorded in backscattering configuration for LNO and LTO single crystals. The tensor elements are defined as in ref. [19].

Scattering configuration	Symmetry species	Tensor element	
		TO	LO
$x(y,y)\ \bar{x}$	A_1-TO, E-TO	a^2+c^2	–
$x(y,z)\ \bar{x}$	E-TO	d^2	–
$x(z,y)\ \bar{x}$	E-TO	d^2	–
$x(z,z)\ \bar{x}$	A_1-TO	b^2	–
$y(x,x)\ \bar{y}$	A_1-TO, E-LO	a^2	c^2
$y(x,z)\ \bar{y}$	E-TO	d^2	–
$y(z,x)\ \bar{y}$	E-TO	d^2	–
$y(z,z)\ \bar{y}$	A_1-TO	b^2	–
$z(x,x)\ \bar{z}$	A_1-LO, E-TO	2^2	a^2
$z(x,y)\ \bar{z}$	E-TO	c^2	–
$z(y,x)\ \bar{z}$	E-TO	c^2	–
$z(y,y)\ \bar{z}$	A_1-LO, E-TO	c^2	a^2

The tensors can be found elsewhere.[17,19,24,41] The scattering geometry in Raman spectroscopy is described with Porto's notation: $k_i(e_i,e_s)k_s$. The vectors k_i and k_s mark the direction of the incident and scattered light in crystal coordinates, respectively, while e_i and e_s label its electric field orientation, i.e., the polarization, also in crystal coordinates. **Table 1** summarizes the 12 possible scattering geometries in backscattering Raman spectroscopy, i.e., $k_i = -k_s = \overline{k_i}$.

The selection rules in (FT)IR spectroscopy are more straightforward. Here, A_1-type symmetry phonons are excited, when the incident and scattered light is polarized parallel to the extraordinary axis (z-axis) of the crystal, i.e., E$\|x$. In contrast, the E-type phonon contributions to the dielectric response are observed when the incident light is polarized parallel to the ordinary crystal axis (xy-plane), i.e., E$\|x$ or E$\|y$. These selection rules are summarized in **Table 2**. Note that the dielectric tensor ε of the LNT crystal family has only two independent components.

3. Density Functional Perturbation Theory

3.1. Computational Details

Phonon eigenmodes, eigenfrequencies, and effective charges are calculated within density functional perturbation theory (DFPT) as implemented in VASP[42–44] and postprocessed by Phonopy,[45,46] an open source python package created for performing basic phonon calculations at the harmonic level. The dielectric function is calculated within the independent particle approximation using the same software. Projector augmented wave potentials[47,48] with exchange–correlation functional in the formulation of Perdew–Burke–Ernzerhof revised for solids (PBEsol)[49,50] and electronic configurations $1s^22s^1$, $4s^24p^64d^35s^2$, $5p^65d^36s^2$, and $2s^22p^4$ for Li, Nb, Ta, and O, respectively, are used. Rhombohedral, primitive unit cells with R3c symmetry model the ferroelectric phase of LNO and LTO, respectively. The used equilibrium lattice parameters are $a_{LT} = 5.474$ Å and $\alpha_{LT} = 56.171°$ for LTO, as well as $a_{LN} = 5.494$ Å and $\alpha_{LN} = 55.867°$ for LNO. These values are in close agreement with the measured lattice parameters.[19,41,51] The ionic positions are optimized, such that all forces acting on the ions are lower than 0.005 eV Å^{-1}. A $8 \times 8 \times 8$ Monkhorst–Pack K-point mesh[52] and an energy cutoff at 500 eV are needed to converge electronic energies to 10 meV. A Gaussian smearing with width 0.05 eV is applied to the Fermi occupancies. Forty-six conduction bands are considered to obtain a dielectric function converged up to 10 eV.

LNT solid solutions are modeled with special quasirandom structures (SQS) created as described in refs. [53–55]. This approach is an improvement over previous works, as it does not only provide a means to accurately simulate the LNT solid solutions with random occupations of the Nb/Ta sites, but it also intrinsically includes local-site deformations, which are important for the accurate simulation of the lattice dynamics of the system. In particular, $1 \times 1 \times 2$ repetitions of the orthorhombic unit cell are employed as supercells to model solid solutions containing a 70.8% Ta concentration. $4 \times 4 \times 1$ Monkhorst–Pack K-point meshes are used, leading to a similar K-point density as for the unit cells. The cell parameters are determined by optimizing the lattice for different volumes and fitting the resulting energies to the Murnaghan equation of state.[56] The number of conduction bands used for the calculation of the electronic contribution to the dielectric function is chosen to obtain the same conduction/valence ratio as for the primitive cells when modeling the end compounds LNO and LTO. Three different SQS are employed for the calculations presented in this work. The de facto equivalence of these SQS is verified by comparing their calculated Raman signals. As shown in **Figure 2**, the calculated spectra only differ marginally. This confirms that the SQS well describe the same material, even though their atomistic distribution is different. Therefore, only one SQS is used as a reference throughout this work. For the mixed crystals, the additional effect of phonons folding back onto the Γ-point has to be taken into account: Because a supercell is needed to describe the random alloy, there will be many more phonon modes present in their calculations. This will lead, in general, to more peaks in the spectra. Here, however, some of these folded modes lie so close to each other in their frequencies that the applied Gaussian smearing will result in fewer, but broader peaks in the spectrum (see Figure 2b). The arguments regarding group theory mentioned in Section 2.4 for the end compounds, strictly speaking, do not apply for the mixed crystals. Therefore, we denote the maxima instead with primed labels. For example, the frequency A_1'-TO_1 represents all modes that contribute to a single peak, which behaves comparable to the A_1-TO_1 in the end compounds.

Table 2. Observable phonon modes recorded for light polarization (electric field) with respect to the crystal axes of LNO or LTO.

Light polarization (E-field)	Symmetry species
E$\|z$	A_1
E$\|y$	E
E$\|x$	E

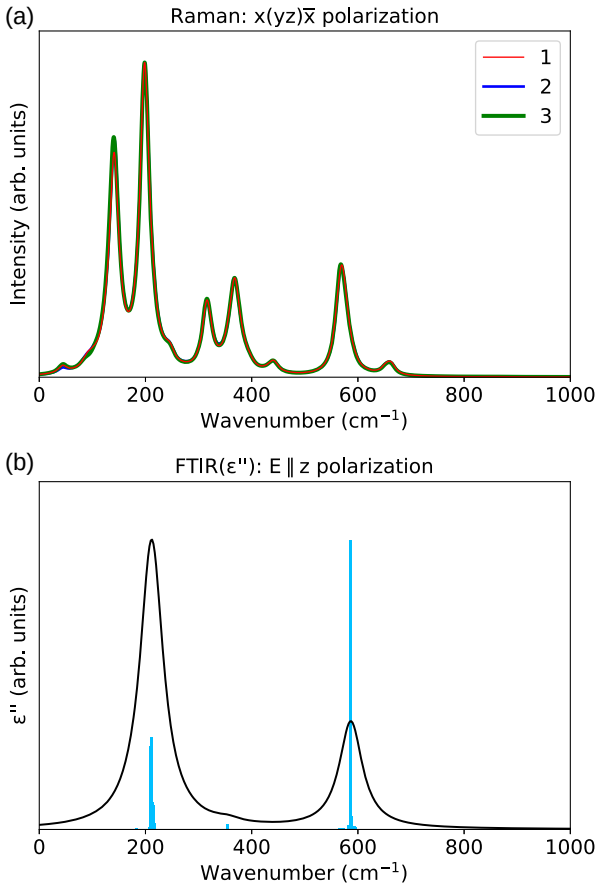

Figure 2. a) Calculated Raman spectra in $x(yz)\bar{x}$ polarization for three different SQS (labeled by the numbers (1–3) of $LiNb_{0.292}Ta_{0.708}O_3$. Red corresponds to the configuration which is used for all subsequent comparisons. b) Imaginary part of the dielectric function of LNT calculated for light polarized along the extraordinary crystal axis (*z*-axis). The blue bars denote the contribution of single-phonon modes to the complete spectrum in arbitrary units.

Even though these frequencies do not hold any information regarding a displacement pattern (except for their symmetry), their frequencies open up an interpretation regarding the Ta content of a given sample. Shifts in frequency depending on the Ta content have been explained in ref. [19]: For most modes, LNO features higher mode frequencies, which can be explained by the mass difference of niobium (92.906 a.u.) as compared to tantalum (180.948 a.u.). Exceptions to this rule are modes involving mostly a movement of the oxygen cage (e.g., A_1-TO_3 and high-frequency E-modes): Here, the shorter Ta—O bond length compared to Nb—O suggests a stronger bond, which results in higher frequencies in LTO for these modes.

3.2. IR Spectra

In Raman or FTIR spectroscopy not only phonon frequencies but also the scattering efficiencies or oscillator strength, respectively, are probed. For an accurate comparison of theoretical and experimental data, therefore, not only the exact frequencies but equally the relative intensities need to be calculated, which proved extremely valuable in the past in assignment of phonon features.[20,31]

(FT)IR spectroscopy directly probes the real and imaginary parts of the dielectric function ε of a material in the respective phonon frequency range, i.e., the direct contribution of the vibrating lattice to the dielectric response. The dipole moment p of a crystal is defined as

$$p = \sum_{\mathrm{b}} \left(\sum_{i,\mathrm{a}} Z_{i\mathrm{ab}} r_i \hat{e}_{\mathrm{a}} \right) \hat{e}_{\mathrm{b}} \tag{2}$$

where r_i denotes the position of ion i and Z_i is its effective charge tensor (i.e., the Born charge). The vectors $\hat{e}_{\mathrm{a,b}}$ label the cartesian unit vectors and the indices a,b the cartesian coordinates. The change of p with respect to a phonon with eigenmode Q can be approximated by a symmetric difference quotient

$$\frac{\partial p}{\partial Q} \sim \sum_{\mathrm{b}} \left(\sum_{i,\mathrm{a}} Z_{i\mathrm{ab}} Q_i \hat{e}_{\mathrm{a}} \right) \hat{e}_{\mathrm{b}} \tag{3}$$

where Q_i denotes the movement of ion i within the displacement pattern Q. The imaginary part of the ionic contribution to the dielectric function can then be calculated as in ref. [57]

$$\begin{aligned} \Im(\varepsilon^{\mathrm{ion}}_{\mathrm{ab}}(\omega_m)) &\sim \left(\frac{\partial p_{\mathrm{a}}}{\partial Q}\right)\left(\frac{\partial p_{\mathrm{b}}}{\partial Q}\right)^* \\ &= \left(\sum_{i,\mathrm{a}'} Z_{i\mathrm{a}'\mathrm{a}} Q_i \hat{e}_{\mathrm{a}'}\right)\left(\sum_{i,\mathrm{a}'} Z_{i\mathrm{a}'\mathrm{b}} Q_i \hat{e}_{\mathrm{a}'}\right)^* \end{aligned} \tag{4}$$

with ω_m being the TO frequency of mode m with displacement pattern Q. The contribution of all phonon modes to the IR spectra is obtained by calculating the sum over all modes m. In the harmonic approximation, these contributions will only yield delta peaks at the TO phonon frequencies ω_m. The real part of the ionic contribution to the dielectric function can be obtained as shown in ref. [57].

3.3. Raman Spectra

In contrast to FTIR, Raman spectroscopy is an inelastic scattering technique, where a photon at much higher energies, typically in the visible range, exchanges energy with a phonon. Subsequently, a photon at a shifted frequency is emitted. This second-order effect is mediated via the electronic contribution of the dielectric response. The Raman tensor α is defined as the change of the polarizability with respect to a phononic eigenmode Q

$$\alpha_{m,\mathrm{ab}}(\omega) = \frac{\partial \varepsilon^{\mathrm{el}}_{\mathrm{ab}}(\omega)}{\partial Q} \sim \varepsilon^{\mathrm{el}}_{R_+,\mathrm{ab}}(\omega) - \varepsilon^{\mathrm{el}}_{R_-,\mathrm{ab}}(\omega) \tag{5}$$

with $\varepsilon^{\mathrm{el}}(\omega)$ being the electronic contribution to the dielectric function and ω the frequency of the incident laser light. Here, we calculate the derivative evaluating $\varepsilon^{\mathrm{el}}$ at two opposite, symmetric ionic displacements $R_{\pm}$. The electronic contribution to the dielectric function is calculated within the independent particle approximation.[58] Using Kramers–Kronig relations, we can

obtain the real part of the electronic contribution to the dielectric function.

The intensity of the Raman signal can be finally calculated as

$$I_m(\omega)[s(\mathrm{ab})i] \sim |\hat{e}_s \alpha_{m,\mathrm{ab}}(\omega)\hat{e}_i|^2 \frac{(\omega-\omega_m)^4}{\omega_m}(n+1) \tag{6}$$

where $\hat{e}_i$ and $\hat{e}_s$ denote the polarization of the incident and scattered light, respectively, and n is the Bose–Einstein distribution.

In contrast to the theoretical data, the experimental spectra are subject to finite line width, due to thermal broadening, resolution limits, or crystal defects. This is not captured in our calculations. Therefore, artificial Gaussian smearings of 5 cm^{-1} width are applied to the calculated spectral intensities (both IR and Raman) to obtain spectra readily comparable to the measured data.

3.4. LO–to Splitting

In order to calculate LO–TO splitting of phonon frequencies at the Γ-point, a dipole–dipole interaction term is added to the dynamical matrix, which reads as[57,59]

$$\frac{1}{\sqrt{m_j m_{j'}}}\frac{4\pi}{V_0}\frac{\left(\sum_c Z_{jca}\hat{q}_c\right)\left(\sum_c Z_{jcb}\hat{q}_c\right)}{\sum_{cc'}\hat{q}_c \varepsilon_{\infty,cc'}\hat{q}_{c'}} \tag{7}$$

where $\hat{q}$ denotes a normalized reciprocal vector, m_j is the mass of ion j, and Z denotes the effective charge tensor of ion j. The letters a, b, c, and c' denote cartesian indices. ε_∞ is the electronic contribution of the static dielectric function. Since all these variables were already calculated in order to obtain IR and Raman spectra, this comes at almost no additional computational cost.

3.5. Phenomenological Model

The generalized LST relation[33,34] can be employed to estimate the phononic contribution to the material's optical response in an approximate manner. The generalized LST connects the high-frequency permittivity ε_∞ to the static permittivity ε_0 through

$$\varepsilon_0 = \varepsilon_\infty \prod_{j=1}^{n} \frac{\omega_{\mathrm{LO}j}^2}{\omega_{\mathrm{TO}j}^2} \tag{8}$$

This is very valuable because the high-frequency dielectric function can be readily calculated from the electronic structure within DFT, but the calculation of the vibrational contributions in the limit of low frequencies—and therefore the static permittivity—is more challenging.

4. Results

4.1. Experimental Results

To unambiguously identify and assign all phonon modes in the LNT material family, the measured experimental data, for both Raman and FTIR spectroscopy, were systematically analyzed and compared while considering the selection rules listed in Table 1 and 2. To illustrate both the process of comparing different Raman spectra and the comparison of Raman and FTIR data, **Figure 3** shows several datasets obtained on the LNO sample. All spectra shown contain signatures of E-type phonons, including both LO and TO modes. In detail, subfigure (a) displays a Raman spectrum in $y(x,x)\bar{y}$ scattering configuration, which according to the selection rules shows E-LO and A_1-TO modes, while (b) shows a Raman spectrum in the crossed configuration $y(z,x)\bar{y}$, which only addresses E-TO phonons. These Raman spectra are compared with c), the real part ε', and d) the imaginary part ε'' of the ordinary-polarized dielectric function extracted from FTIR spectroscopy using the fitting process shown in Figure 1.

To extract phonon frequencies from the FTIR data, several possibilities exist. In principle, fitting the FTIR data with a four parameter model, as above, yields not only a dielectric function but also the LO and TO frequencies for each phonon, which can be readily compared to the Raman and theory data. However, due to the strong overlap of many phonons in the 200–500 cm^{-1} range, the determined phonon frequencies in particular for the weakly scattering phonons have a large uncertainty and ambiguity in the fit. This is observed more pronounced in the LO frequencies. The main goal of the fitting procedure is to obtain a complex dielectric function to best describe the reflectance spectrum. Another way to identify the frequencies is by analyzing the real and imaginary parts of the dielectric function, where the LO and TO frequencies manifest themselves in a specific way: Here, the maximum of the imaginary part of the dielectric function corresponds to the TO frequencies, which also corresponds to the fitted TO frequency. In contrast, the LO frequencies manifest themselves in a more subtle way in the dielectric function. The LO frequencies generally describe the high-frequency end of each phonon's Reststrahlen band, where the real part of dielectric function equals zero when crossing from negative to positive values (zero crossing with an upward slope). Therefore, we label these zero crossing of the real part of the dielectric function with the respective LO frequency instead of using the fitted parameters. Note that the zero crossing from positive-to-negative (downward slope) values is equivalent to the TO frequencies, where also the imaginary part of the dielectric function has its maximum. This labeling procedure is equivalent to previous works when identifying the LO modes when fitting a three parameter model, where no specific LO frequency is fitted and instead the dielectric function needs to be analyzed. Due to the overlaps in the 200–500 cm^{-1} range, not all phonons lead to a zero crossing of the total dielectric function. Therefore, only those modes which result in a visible zero crossing are considered to determine the respective LO frequencies, while the weaker ones typically yield higher uncertainties.

In contrast to the real part, the imaginary part of the dielectric function resembles in its structure an emission-type spectrum with peaks centered at the TO frequencies. This structure looks very similar to the Raman spectrum of TO phonons, which therefore allows a direct visual comparison. Note that while the spectra have a similar shape, the spectra originate from different physical processes, i.e., a phonon with a strong absorption in the dielectric function does not necessarily mean a high scattering efficiency in Raman scattering.

In the cross-polarized Raman spectrum in Figure 3b), eight peaks can be identified. Out of these, seven belong to E-TO phonons, while the peak at 633 cm^{-1} belongs to the A_1-TO_4 that is

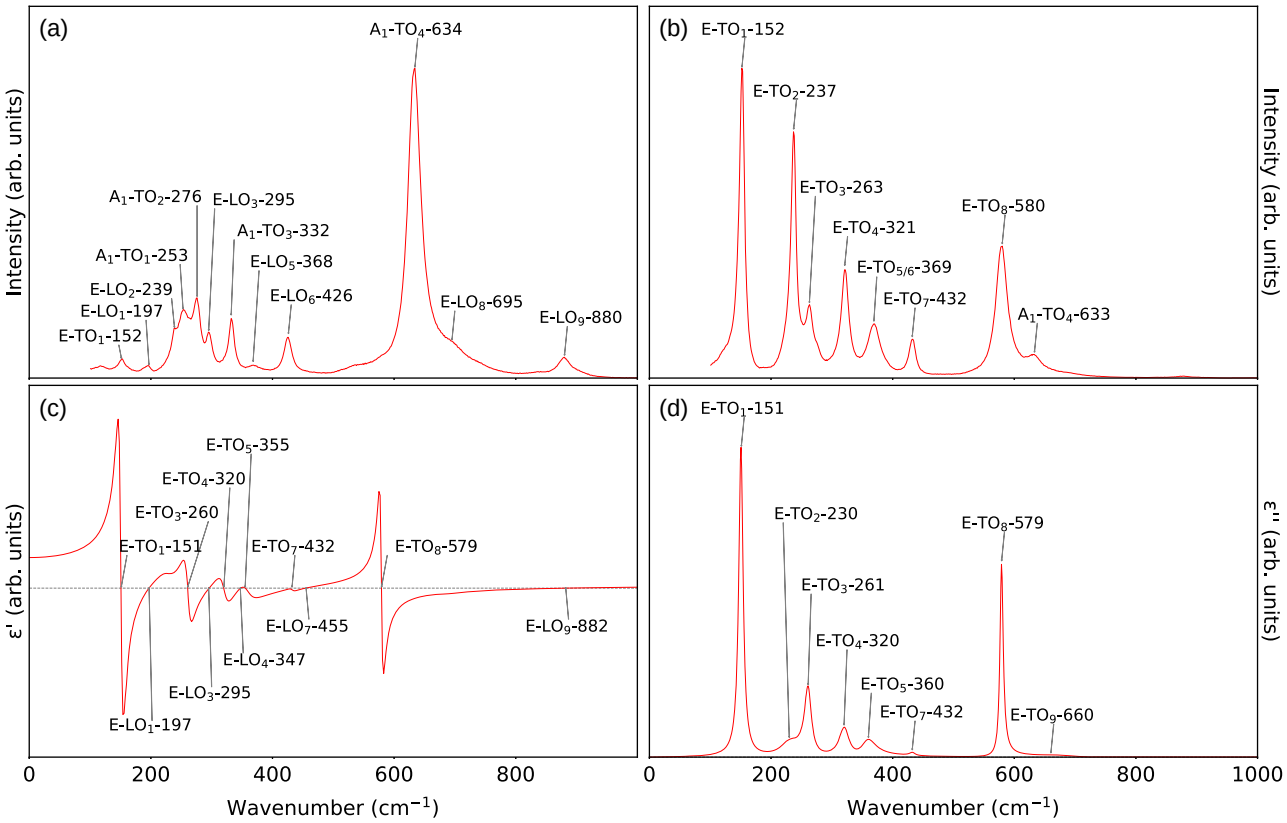

Figure 3. (Top) a) Raman spectra of LNO for polarization $y(xx)\bar{y}$ (left) and b) $y(zx)\bar{y}$ (right). (Bottom) c) Real and d) imaginary part of the dielectric function for light polarized along the crystallographic *x*-direction, extracted from FTIR spectra. All spectra are normalized with respect to their highest peak. In the Raman spectra, the A_1-TO and E-LO modes (a) as well as the E-TO modes (b) can be assigned by applying the symmetry considerations from Table 1. The E-LO modes can be extracted as zero crossings in ε'. Additionally, the E-TO modes can be extracted from peak positions in ε'' (d). The redundancies in these four graphics serve as an appraisal for the measurements and calculations.

not fully suppressed by the analyzer. In detail, the visible peaks belong to the E-TO_1, -TO_2, -TO_3, -TO_4, -$TO_{5/6}$, -TO_7, and –TO_8 modes. Similarly, the imaginary dielectric function shows six relatively strong peaks (E-TO_1, -TO_2, -TO_3, -TO_4, -TO_5, and -TO_8) and two very weak, but identifiable peaks (E-TO_7, -TO_9). Here, it can be seen that the E-TO_9 at 660 cm^{-1} has a very weak intensity in both Raman and FTIR, which was previously observed as well[19,20,24] and is also found in the DFPT calculations (Figure S1, Supporting Information). Its behavior is different from its behavior in LTO, where the E-TO_9 has a much stronger scattering efficiency in Raman spectroscopy, but is still very weak in FTIR spectroscopy (see **Figure 4** and Figure S4, Supporting Information). Due to its low scattering efficiency, the E-TO_9 mode was often assigned ambiguously in the past.[19,20,24,31] Further, it can be noticed that the E-TO_5 and E-TO_6 frequencies are very close (360 cm^{-1} vs 367 cm^{-1}). While the TO_6 is dominating in Raman scattering, the TO_5 is the dominating feature for the FTIR spectrum. Previous work has indicated that the scattering efficiency and their behavior in both phonons are similar for both LTO and mixed crystals. As a result, the Raman and FTIR spectra were only fitted with one peak representing the TO_5 or TO_6 mode, respectively. Only low-temperature measurements of stoichiometric crystals allow to unambiguously differentiate these modes in Raman spectroscopy.[24] The origin in the different scattering efficiencies for both phonons and in both methods is also backed up by the DFPT calculations discussed below. Overall, the E-TO phonon frequencies determined from different Raman spectra, as well as by comparing FTIR and Raman spectra, match within ±5 cm^{-1}, which is in agreement with the combined resolution limits of both methods.

The spectrum in Figure 3a) shows a Raman spectrum in $y(x,x)\bar{y}$ configuration, which shows both E-LO and A_1-TO phonons. The A_1-TO phonons are dominating in intensity. Here, they have a strong scattering efficiency leading to strong overlaps in the 200–400 cm^{-1} region. The A_1-TO phonon peaks can be readily excluded by comparison with spectra in $x(z,z)\bar{x}$ (Figure S2a, Supporting Information) or $x(y,y)\bar{x}$ configurations (e.g., Figure S1a, Supporting Information). The remaining peaks, therefore, are exclusively E-LO phonons. E-LO phonons are only accessible in this single-scattering configuration for back scattering, which in the past led to the most ambiguity in assignment for this phonon branch.[24,31] Therefore, the comparison to the real part of the dielectric function (and to the calculations) is particular helpful for a correct assignment. Again, by comparison, a good agreement is found and all nine E-LO phonons can be identified and a frequency can be determined.

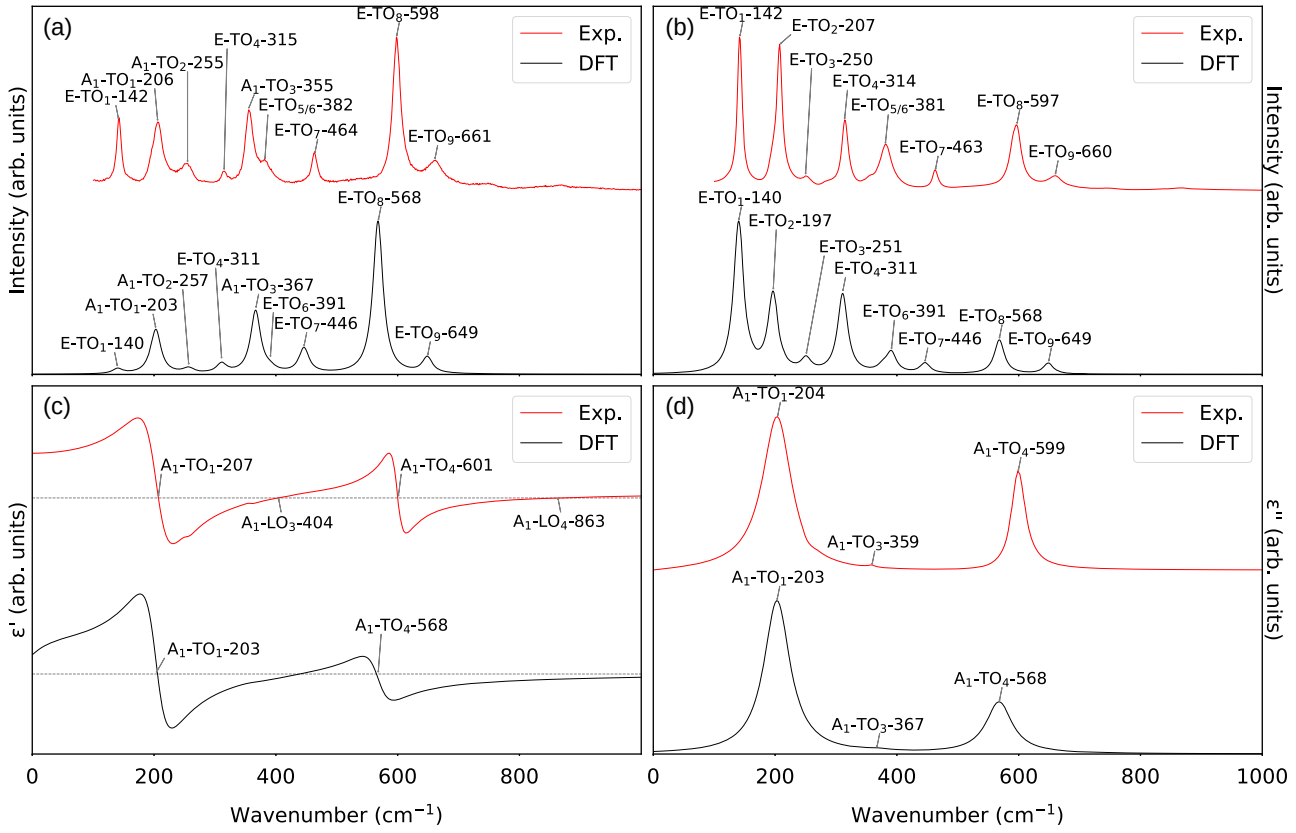

Figure 4. (Top) a) Raman spectra of LTO for polarization $x(yy)\bar{x}$ (left) and b) $x(zy)\bar{x}$ (right). (Bottom) c) Real and d) imaginary dielectric functions for light polarized along the crystallographic *z*-direction, extracted from FTIR spectra. All spectra are normalized with respect to their highest peak. In the Raman spectra, the A_1-TO and E-TO modes can be unambiguously assigned by applying the symmetry considerations from Table 1. The A_1-LO modes can be extracted as zero crossings or poles in ε'. The redundancies in these four graphics serve as an appraisal for the measurements and calculations.

Similar to the discussion above, the Raman and FTIR data for all samples, LNO, LTO, and LNT, were evaluated for different cuts. Additional plots and tabular summaries of all phonon frequencies are available in the Supporting Information. These tables denote the mean phonon frequencies, determined by analyzing all our Raman and FTIR spectra for all available crystal cuts. In the next step, the experimental data will be compared exemplarily with the calculations from DFPT.

4.2. Comparison Between Theory and Experiment

The calculated and measured TO phonon frequencies of LNO and LTO are given in Tables SI and SII, Supporting Information, respectively. As the A_2 modes are Raman and IR silent for ideal crystals, we just report the calculated frequencies, although—as seen below—we may see indications of those phonons activated in the measured spectra due to defects or stoichiometry. A detailed discussion of the difference in frequencies for the same modes in LNO and LTO is given in the previous work[19] and will not be repeated here. Here, we will specifically focus on the calculated spectra for both the dielectric function and Raman signal. Because we only calculated Raman and FTIR spectra for TO frequencies, we limit our comparison of Raman spectra to the $x(..)\bar{x}$ configuration.

Overall, the calculated and measured TO phonon frequencies are all in good agreement with each other and lay mostly within the accuracy of both experimental setups, as well as with available previous computational and experimental results.[20,24,31,60] The largest deviation for LNO occurs for the E-TO_2 mode with a discrepancy of around 6% (14 cm^{-1}) (see, e.g., **Figure 5**a or Table SI, Supporting Information). The overall small deviations in frequency between experiment and theory is mostly caused by using fixed lattice constants in the simulations, which are in good agreement to experimental values.

The dielectric functions show the same number of peaks/features and similar intensities in the real and imaginary part for both investigated polarization directions for LNO, LTO, and LNT. We note that the simulated ε' does not allow for an assignment of the LO modes, as no information from the simulation leading to a LO–TO splitting is provided at this point. The peaks and shape of ε' and ε'' do, however, coincide to the experimental data in all cases. Note that the peak width in the calculated data is arbitrarily introduced and knowledge of the damping constants from theory is not available.

The splitting as well as the different Raman and IR activity of the E-TO_5 and E-TO_6 modes can be easily verified by our calculations (e.g., Figure S1 for LNO and Figure S4, Supporting Information for LTO): Here, the E-TO_5 and E-TO_6 modes

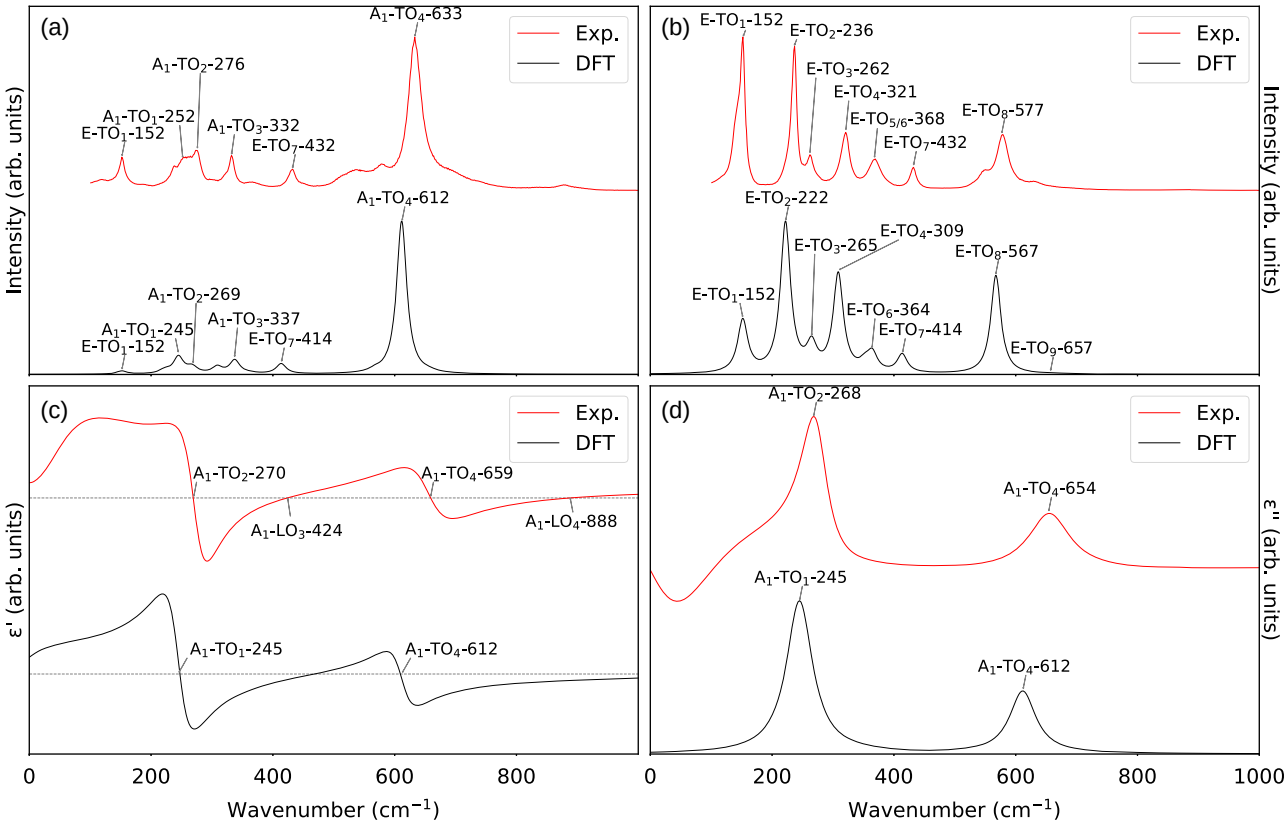

Figure 5. (Top) a) Raman spectra of LNO for polarization $x(yy)\bar{x}$ (left) and b) $x(zy)\bar{x}$ (right). (Bottom) c) Real and d) imaginary part of the dielectric function for light polarized along the crystallographic z-direction, extracted from FTIR spectra. All spectra are normalized with respect to their highest peak. In the Raman spectra, the A_1-TO and E-TO modes can be unambiguously assigned by applying the symmetry considerations from Table 1. The A_1-LO modes can be extracted as zero crossings in ε'. The redundancies in these four graphics serve as an appraisal for the measurements and calculations.

($352\,cm^{-1}$ vs $364\,cm^{-1}$ for LNO) can be clearly separated in the spectra. As observed in the experiment, the E-TO_6 is almost IR inactive (invisible in the spectra), but has a higher Raman activity than E-TO_5, while the inverse statement is true for the E-TO_6.

For better comparison, we increase the Gaussian smearing applied to the calculated spectra for E$\|z$ to $25\,cm^{-1}$, which will lead to broader peaks in, e.g., Figure S2 compared to, e.g., Figure S1, Supporting Information. We expect an overall broadening of the peaks (broader than in the end compounds) for the LNT crystal, regardless of other defects, e.g., Li inhomogeneities, because of the intrinsic presence of folded modes in a random alloy.

The A_1'-TO_4-like mode at $587\,cm^{-1}$ has by far the highest IR activity. However, the peak resulting from the overlap of multiple modes at 210–215 cm^{-1} results in an overall higher signal. Only a single mode at $354\,cm^{-1}$ contributes to the shoulder at the same frequency. Therefore, in general, in the mixed crystals we cannot assign a peak in either the FTIR or Raman signal to a true single phonon eigenmode, but instead assign such a sum feature with a single frequency to its closest analogue in the end compounds and label it with a prime.

Curiously, apart from the expected A_1- and E-type-like phonon modes, we note a significant peak in the calculated and measured Raman spectra for $x(yy)\bar{x}$ polarization (**Figure 6**) at $855\,cm^{-1}$: In the calculations, this peak belongs to a A_2'-TO_5 mode, which is, due to local deformations present in the SQS (leading to a slightly imperfect eigenvector), not completely suppressed. This peak is also visible in the measured spectrum for LNT, and even for LNO and LTO in the same Raman configuration, but it is much less pronounced for the end compounds. Here, this peak could also correspond to a not completely suppressed E-LO_9 or A_1-LO_4 mode. However, its clear presence in the calculated spectra of the solid solution might also indicate that defects in the end compounds or the random Nb–Ta distribution in the mixed crystals can relax the selection rules, which enables the A_2-TO_5 mode to become Raman active. This behavior has been previously observed for LNO and LTO crystals which include impurities and defects.[61]

For our simulations, the LO-mode frequencies cannot be directly extracted from the dielectric function. Instead, we apply Equation (7) for different q-directions and track how the added dipole–dipole interaction affects the mode frequencies at Γ. Our results can be found in Table S III, SIV, and SV, Supporting Information. Note that we do not show A_2 modes in these tables, as they do not show any LO–TO splitting. Overall, the calculated and measured frequencies agree within an error of 9%, where the measured frequencies are for almost all modes slightly larger. This discrepancy can be easily explained by taking a closer look at Equation (7): Because of the underestimation of the electronic bandgap in the DFT calculations (e.g., measured for LNO

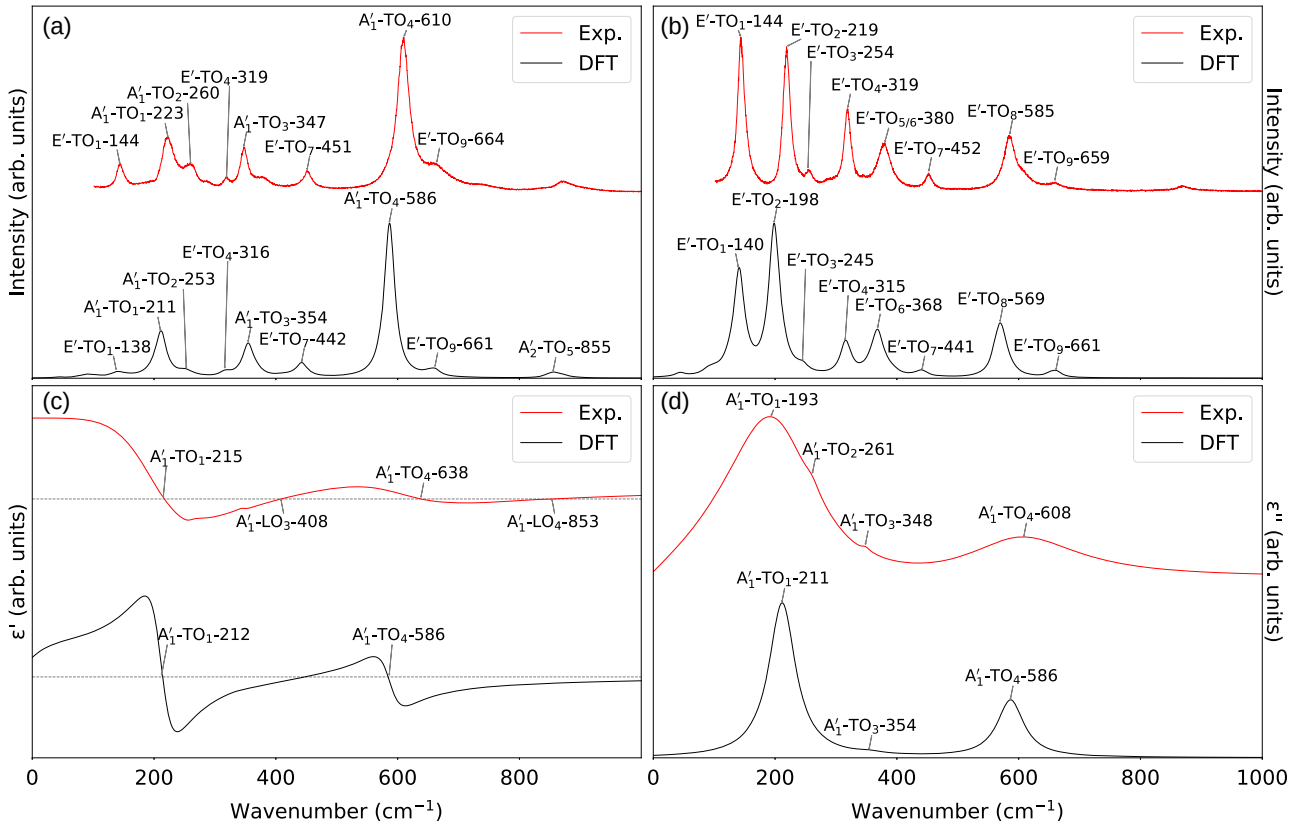

Figure 6. (Top) a) Raman spectra of LNT for polarization $x(yy)\,\bar{x}$ (left) and b) $x(zy)\,\bar{x}$ (right). (Bottom) c) Real and d) imaginary dielectric functions for light polarized along the crystallographic *z*-direction, extracted from FTIR spectra. All spectra are normalized with respect to their highest peak. In the Raman spectra, the A_1-TO and E′-TO modes can be unambiguously assigned by applying the symmetry considerations from Table 1. The A_1-LO modes can be extracted as zero crossings or poles in ε'. The redundancies in these four graphics serve as an appraisal for the measurements and calculations.

3.7 eV[62] vs our DFT calculation with 3.41 eV), a redshift of the imaginary part of the dielectric function is introduced. This, in turn, gives rise to a larger value for ε_∞, as Kramers–Kronig relations are used to calculate the real part. Thus, the added dipole–dipole interaction term is likely underestimated, which in conclusion leads to smaller LO frequencies. Especially large LO–TO splits can be observed for the high-frequency A_1 and E modes (A_1-TO_4–A_1-LO_4 and E-TO_9–E-LO_9): Both of these modes involve a stretching of the oxygen cage as well as slight movement of the niobium/tantalum within it (see **Figure 7**). Because this central ion carries a large effective charge, these movements introduce a strong dipole–dipole interaction, which, in turn, leads to a large LO–TO splitting.

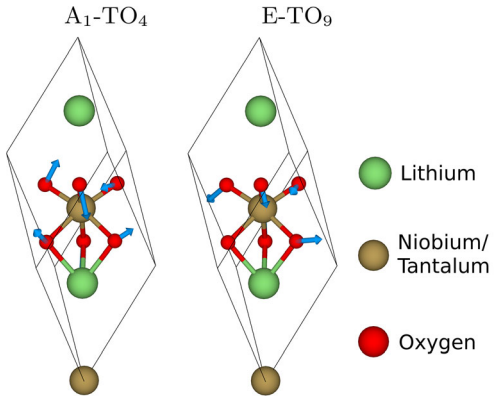

Figure 7. (Left) A_1-TO_4 eigenmode. (Right) E-TO_9 eigenmode. The niobium/tantalum, lithium, and oxygen ions are colored gold, green, and red, respectively. The displacements are denoted by blue arrows.

4.3. Calculation of ε_0

Finally, we use the LST relation to estimate ε_0: From the DFPT calculation, we can extract ε_∞ as the value of ε' at excitation frequency zero. The extracted values for LNO are $\varepsilon_\infty^x = 5.51$ and $\varepsilon_\infty^z = 5.35$. Inserting the calculated values for ε_∞ and phonon frequencies for LNO into Equation (8), we find $\varepsilon_0^x = 40.0$ and $\varepsilon_0^z = 26.0$. Both values are in good agreement to the literature.[19,24,63–65] Using the measured phonon frequencies, we instead obtain $\varepsilon_0^x = 48.9$ and $\varepsilon_0^z = 30.3$, which is slightly larger, however also within the range typically reported in the literature.[19,24,63–65] Repeating the calculations for LTO and LNT, we obtain ε_0 as a function of Ta content (see **Figure 8**). All extracted values, including LTO and LNT, can be found in **Table 3**. Note that the overestimation of ε_∞ leads to slightly higher values of ε_0 compared to the literature. In total, we thus

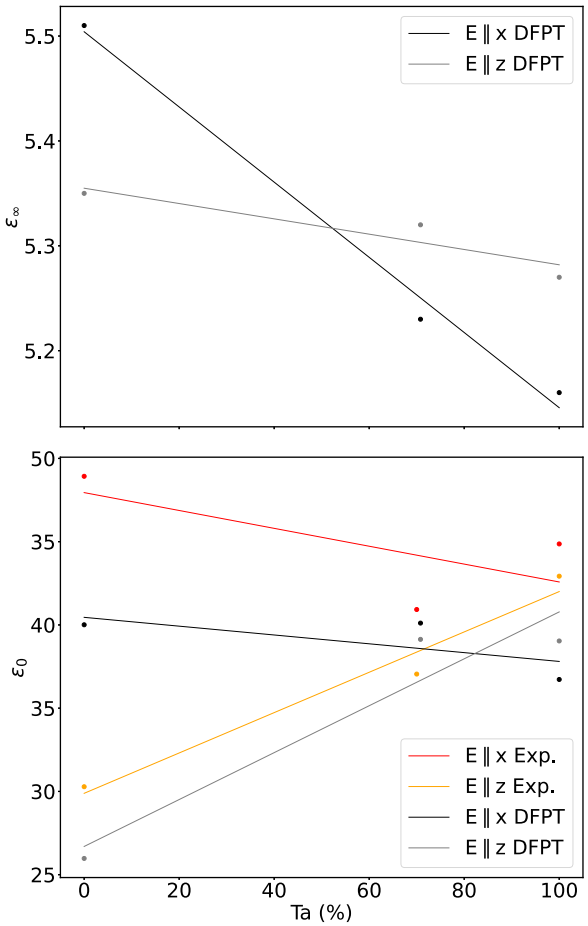

Figure 8. ε_∞ (top) and ε_0 (bottom) as a function of tantalum content of the LNT crystal family. The values for ε_0 are obtained using the LST relation (Equation (8)), whereas ε_∞ is obtained by DFPT calculations. Only polarizations E||*x* and E||*z* are considered. For calculating ε_0, either the measured phonon frequencies (Exp., red and orange) or the calculated ones (DFPT, black and gray) are used.

Table 3. With Equation (8) calculated values for ε_0, using either the calculated frequencies (DFPT) or the measured ones (DFPT + Exp.). Only polarizations E||*x* (*z*-cut) and E||*z* (*x*-cut) are considered. Available data[19,24,63,64] (Ref.) are reported for comparison.

		ε_∞		ε_0		
Crystal	Cut	DFPT	Ref.	DPFT	DFPT + Exp.	Ref.
LNO	*z*	5.51	5.00	40.0	48.9	39.2–42.5
–	*x*	5.35	4.60	26.0	30.3	23.6–26
LTO	*z*	5.16	4.50	36.7	44.9	34.7–42
–	*x*	5.27	4.53	40.0	42.9	35.8–40
LNT	*z*	5.23	4.44	40.1	40.9	36.4
–	*x*	5.32	4.39	36.7	37.0	32.1

suspect our results to be slightly overestimating ε_0. The uncertainty of $\pm 4\ \mathrm{cm}^{-1}$ in the measured frequencies results in an error of around 7% for our obtained values for ε_0.

5. Summary

In this work, we have studied the vibrational properties of the lattice in the LNT material family by studying the end compounds LTO and LNO, as well as an example of a mixed crystal LNT. To achieve a high redundancy in the analysis, we have systematically compared measured Raman spectra and FTIR reflectance spectra, which allows us to extract the real and imaginary parts of the dielectric function, with calculated Raman spectra and dielectric functions obtained from first principles. When applying group symmetry considerations and comparing all resulting spectra (experiment and theory), we can unambiguously assign all transverse optical and longitudinal optical phonon modes at the Brillouin zone center (Γ-point). In particular, by combining both theory and experiment, the similarities and differences in the spectra, as well as their changes within mixed crystals, can be readily explained and interpreted. An example is the different intensity of quasi-silent modes in Raman or FTIR spectra, or even the appearance of symmetry forbidden modes like the A_2-TO_5 in Raman spectra. Here, the experiments and the theoretical calculations are in excellent agreement for all studied samples, demonstrating the high redundancy of this combined approach. Both the theory and experimental data additionally allow us to obtain the phononic contribution to the dielectric function in the full LNT material family by applying the LST. Again, the calculated data are in excellent agreement to previous studies.[19,24,63,64] In principle, this methodology is not limited to the LNO–LTO crystal system, but this tested approach can be readily expanded to other crystals, doped or strained systems, or domain wall spectra,[66–69] where our work thus serves as a baseline for interpreting the underlying physical effects and crystal structure by providing a quantitative interpretation of Raman or FTIR spectra.

Supporting Information

Supporting Information is available from the Wiley Online Library or from the author.

Acknowledgements

F.B., S.G. and A.K. contributed equally to this work. The authors gratefully acknowledge financial support by the Deutsche Forschungsgemeinschaft (DFG) through the DFG research group FOR5044 (grant no. 426703838;[70] https://www.for5044.de). In addition, the TU Dresden team acknowledges the financial support by the Bundesministerium für Bildung und Forschung (BMBF, Federal Ministry of Education and Research, Germany, project grant nos. 05K19ODA, 05K19ODB, and 05K22ODA), as well as by the DFG through projects CRC1415 (ID: 417590517), and the Würzburg-Dresden Cluster of Excellence ct.qmat (EXC 2147, ID: 390858490). Calculations for this research were conducted on the Lichtenberg high-performance computer of the TU Darmstadt and at the Höchstleistungrechenzentrum Stuttgart (HLRS). The authors, furthermore, acknowledge the computational resources provided by the HPC Core Facility and the HRZ of the Justus-Liebig-Universität Gießen.

Open Access funding enabled and organized by Projekt DEAL.

Conflict of Interest

The authors declare no conflict of interest.

Data Availability Statement

The data that support the findings of this study are available from the corresponding author upon reasonable request.

Keywords

density functional theory calculations, Fourier-transform infrared spectroscopy, lithium niobate and lithium tantalite, lithium niobate tantalate solid solutions, Raman spectroscopy

Received: December 21, 2023
Revised: August 12, 2024
Published online: November 21, 2024

[1] R. S. Weis, T. K. Gaylord, *Appl. Phys. A* **1985**, *37*, 191.
[2] A. Räuber, *Current Topics in Materials Science*, Vol. *1*, Elsevier Science Publishing, Amsterdam **1978**.
[3] T. Volk, M. Wöhlecke, *Springer Series in Materials Science*, Vol. *115*, Springer, Berlin Heidelberg **2009**.
[4] S. Sanna, W. G. Schmidt, *IEEE Trans. Ultrason. Ferroelectr. Freq. Control* **2012**, *59*, 1925.
[5] S. R. Phillpot, V. Gopalan, *Appl. Phys. Lett.* **2004**, *84*, 1916.
[6] Y.-L. Chen, J.-J. Xu, X.-J. Chen, Y.-F. Kong, G.-Y. Zhang, *Opt. Commun.* **2001**, *188*, 359.
[7] K. Kitamura, Y. Furukawa, K. Niwa, V. Gopalan, T. E. Mitchell, *Appl. Phys. Lett.* **1998**, *73*, 3073.
[8] T.-C. Lee, J.-T. Lee, M. A. Robert, S. Wang, T. A. Rabson, *Appl. Phys. Lett.* **2003**, *82*, 191.
[9] R. G. Gruenke, O. A. Hitchcock, E. A. Wollack, C. J. Sarabalis, M. Jankowski, T. P. McKenna, N. R. Lee, A. H. Safavi-Naeini, *Sci Rep.* **2024**, *14*, 6663.
[10] S. Sanna, W. G. Schmidt, *J. Phys.: Condens. Matter* **2017**, *29*, 413001.
[11] U. Yakhnevych, C. Kofahl, S. Hurskyy, S. Ganschow, Y. Suhak, H. Schmidt, H. Fritze, *Solid State Ionics* **2023**, *392*, 116147.
[12] M. Nakamura, S. Takekawa, S. Kumaragurubaran, K. Kitamura, *Jpn. J. Appl. Phys.* **2008**, *47*, 3476.
[13] Y. S. Kim, R. T. Smith, *J. Appl. Phys.* **2003**, *40*, 4637.
[14] U. Bashir, K. Böttcher, D. Klimm, S. Ganschow, F. Bernhardt, S. Sanna, M. Rüsing, L. M. Eng, M. Bickermann, *Ferroelectrics* **2023**, *613*, 250.
[15] D. Roshchupkin, R. Fakhrtdinov, B. Redkin, V. Karandashev, V. Khvostikov, A. Mololkin, O. Siminko, A. Zabelin, *J. Cryst. Growth* **2023**, *621*, 127377.
[16] Y. Suhak, D. Roshchupkin, B. Redkin, A. Kabir, B. Jerliu, S. Ganschow, H. Fritze, *Crystals* **2021**, *11*, 398.
[17] A. Bartasyte, S. Margueron, A. M. Glazer, E. Simon, I. Gregora, S. Huband, P. A. Thomas, *Phys. Rev. B* **2019**, *99*, 094306.
[18] I. G. Wood, P. Daniels, R. H. Brown, A. M. Glazer, *J. Phys.: Condens. Matter* **2008**, *20*, 235237.
[19] M. Rüsing, S. Sanna, S. Neufeld, G. Berth, W. G. Schmidt, A. Zrenner, H. Yu, Y. Wang, H. Zhang, *Phys. Rev. B* **2016**, *93*, 184305.
[20] S. Sanna, S. Neufeld, M. Rüsing, G. Berth, A. Zrenner, W. G. Schmidt, *Phys. Rev. B* **2015**, *91*, 224302.
[21] M. Friedrich, A. Schindlmayr, W. G. Schmidt, S. Sanna, *Phys. Status Solidi B* **2016**, *253*, 683.
[22] V. Caciuc, A. V. Postnikov, *Phys. Rev. B* **2001**, *64*, 224303.
[23] C. Raptis, *Phys. Rev. B* **1988**, *38*, 10007.
[24] S. Margueron, A. Bartasyte, A. M. Glazer, E. Simon, J. Hlinka, I. Gregora, J. Gleize, *J. Appl. Phys.* **2012**, *111*, 104105.
[25] M. Friedrich, A. Riefer, S. Sanna, W. G. Schmidt, A. Schindlmayr, *J. Phys.: Condens. Matter* **2015**, *27*, 385402.
[26] A. Ridah, P. Bourson, M. D. Fontana, G. Malovichko, *J. Phys.: Condens. Matter* **1997**, *9*, 9687.
[27] X. Yang, G. Lan, B. Li, H. Wang, *Phys. Status Solidi B* **1987**, *142*, 287.
[28] K. Parlinski, Z. Q. Li, Y. Kawazoe, *Phys. Rev. B* **2000**, *61*, 272.
[29] C. A. Gautier, M. Mérian, J. Etchepare, *J. Phys.: Condens. Matter* **2000**, *12*, 7175.
[30] R. Claus, G. Borstel, E. Wiesendanger, L. Steffan, *Phys. Rev. B* **1972**, *6*, 4878.
[31] P. Hermet, M. Veithen, P. Ghosez, *J. Phys.: Condens. Matter* **2007**, *19*, 456202.
[32] S. Sanna, A. Riefer, S. Neufeld, W. G. Schmidt, G. Berth, M. Rüsing, *Ferroelectrics* **2013**, *447*, 63.
[33] R. H. Lyddane, R. G. Sachs, E. Teller, *Phys. Rev.* **1941**, *59*, 673.
[34] A. Chaves, S. Porto, *Solid State Commun.* **1973**, *13*, 865.
[35] Y. Saito, M. Kobayashi, D. Hiraga, K. Fujita, S. Kawano, N. I. Smith, Y. Inouye, S. Kawata, *J. Raman Spectrosc.* **2008**, *39*, 1643.
[36] S. Reitzig, F. Hempel, J. Ratzenberger, P. A. Hegarty, Z. H. Amber, R. Buschbeck, M. Rüsing, L. M. Eng, *Appl. Phys. Lett.* **2022**, *120*, 162901.
[37] A. S. Barker, A. A. Ballman, J. A. Ditzenberger, *Phys. Rev. B* **1970**, *2*, 4233.
[38] F. Gervais, B. Piriou, *J. Phys. C: Solid State Phys.* **1974**a, *7*, 2374.
[39] F. Gervais, B. Piriou, *Phys. Rev. B* **1974**b, *10*, 1642.
[40] A. B. Kuzmenko, *Rev. Sci. Instrum.* **2005**, *76*, 083108.
[41] A. Bartasyte, A. Glazer, F. Wondre, D. Prabhakaran, P. Thomas, S. Huband, D. Keeble, S. Margueron, *Mater. Chem. Phys.* **2012**, *134*, 728.
[42] G. Kresse, J. Hafner, *Phys. Rev. B* **1993**, *47*, 558.
[43] G. Kresse, J. Furthmüller, *Mater. Phys.* **1996**a, *54*, 11169.
[44] G. Kresse, J. Furthmüller, *Comput. Mater. Sci.* **1996**b, *6*, 15.
[45] A. Togo, L. Chaput, T. Tadano, I. Tanaka, *J. Phys. Condens. Matter* **2023**, *35*, 353001.
[46] A. Togo, *J. Phys. Soc. Jpn.* **2023**, *92*, 012001.
[47] P. E. Blöchl, *Phys. Rev. B* **1994**, *50*, 17953.
[48] D. Joubert, *Mater. Phys.* **1999**, *59*, 1758.
[49] J. P. Perdew, K. Burke, M. Ernzerhof, *Phys. Rev. Lett.* **1996**, *77*, 3865.
[50] J. P. Perdew, A. Ruzsinszky, G. I. Csonka, O. A. Vydrov, G. E. Scuseria, L. A. Constantin, X. Zhou, K. Burke, *Phys. Rev. Lett.* **2008**, *100*, 136406.
[51] S. Huband, D. S. Keeble, N. Zhang, A. M. Glazer, A. Bartasyte, P. A. Thomas, *J. Appl. Phys.* **2017**, *121*, 024102.
[52] J. D. Pack, H. J. Monkhorst, *Phys. Rev. B* **1977**, *16*, 1748.
[53] S.-H. Wei, L. G. Ferreira, J. E. Bernard, A. Zunger, *Phys. Rev. B* **1990**, *42*, 9622.
[54] J. von Pezold, A. Dick, M. Friák, J. Neugebauer, *Phys. Rev. B* **2010**, *81*, 094203.
[55] A. van de Walle, P. Tiwary, M. de Jong, D. Olmsted, M. Asta, A. Dick, D. Shin, Y. Wang, L.-Q. Chen, Z.-K. Liu, *Calphad* **2013**, *42*, 13.
[56] V. G. Tyuterev, N. Vast, *Comput. Mater. Sci.* **2006**, *38*, 350.
[57] X. Gonze, C. Lee, *Phys. Rev. B* **1997**, *55*, 10355.
[58] M. Gajdoš, K. Hummer, G. Kresse, J. Furthmüller, F. Bechstedt, *Phys. Rev. B* **2006**, *73*, 045112.
[59] X. Gonze, J.-C. Charlier, D. Allan, M. Teter, *Phys. Rev. B* **1994**, *50*, 13035.
[60] Y. Repelin, E. Husson, F. Bennani, C. Proust, *J. Phys. Chem. Solids* **1999**, *60*, 819.
[61] V. S. Gorelik, N. V. Sidorov, A. I. Vodchits, *Phys. Wave Phenom.* **2017**, *25*, 10.
[62] A. Dhar, A. Mansingh, *J. Appl. Phys.* **1990**, *68*, 5804.
[63] A. S. Barker, R. Loudon, *Phys. Rev.* **1967**, *158*, 433.
[64] M. Veithen, P. Ghosez, *Phys. Rev. B* **2002**, *65*, 214302.
[65] T. Fujii, A. Ando, Y. Sakabe, *J. Eur. Ceram. Soc.* **2006**, *26*, 1857.

[66] M. Rüsing, S. Neufeld, J. Brockmeier, C. Eigner, P. Mackwitz, K. Spychala, C. Silberhorn, W. G. Schmidt, G. Berth, A. Zrenner, S. Sanna, *Phys. Rev. Mater.* **2018**, *2*, 103801.
[67] G. F. Nataf, N. Barrett, J. Kreisel, M. Guennou, *J. Phys.: Condens. Matter* **2017**, *30*, 035902.
[68] P. S. Zelenovskiy, V. Y. Shur, P. Bourson, *Ferroelectrics* **2010**, *398*, 34.
[69] M. D. Fontana, R. Hammoum, P. Bourson, S. Margueron, V. Y. Shur, *Ferroelectrics* **2008**, *373*, 26.
[70] S. Ganschow, H. Schmidt, Y. Suhak, M. K. Imlau, M. Rüsing, L. M. Eng, H. Fritze, S. Sanna, Periodic Low-Dimensional Defect Structures in Polar Oxides, https://www.for5044.de (accessed: October 2021).